1st IAA Conference on Space Situational Awareness (ICSSA)

Orlando, FL, USA

IAA-ICSSA-17-01-06

REMOVAL OF ORBITAL DEBRIS FROM GEOSTATIONARY ORBITS USING SOLAR RADIATION PRESSURE AND LYAPUNOV CONTROL

Patrick W. Kelly[1], **Riccardo Bevilacqua**[1], **Leonel Mazal**[1], and **Richard S. Erwin**[(2)]

[(1)] *University of Florida, 939 Sweetwater Drive, MAE-A 211, Gainesville FL, 32611, (352)846-1477, pkelly89@ufl.edu, bevilr@ufl.edu, leo.mazal@ufl.edu*

[(2)] *Air Force Research Laboratory, 3550 Aberdeen Ave. SE, Kirtland AFB NM, 87117-5776,(505)846-9816, richard.erwin@us.af.mil*

Keywords: *Solar Radiation Pressure, Orbital Debris, Solar Sail, Lyapunov Control, Geostationary Orbit*

The accumulation of space debris continues to grow as commercial space applications become more affordable and existing satellites approach the end of their operational lifetimes. To protect global interests in current and future satellite missions, the Inter-Agency Debris Coordination Committee (IADC) has established guidelines for proper disposal of retired satellites. Based on these guidelines, we propose a satellite concept called TugSat to assist in the removal of satellites from geosynchronous equatorial orbits (GEO) using the effects of solar radiation pressure (SRP). Solar radiation pressure is the dominant non-gravitational perturbation in the GEO belt and can be directed deliberately using large, high-performance solar sails. Using sail orientations derived from Lyapunov functions, a solar-sailing CubeSat can be tasked to deorbit satellites on the order of 1000 kg using the current state of the art in solar sailing technology. Due to this reliance on SRP, the TugSat CubeSat can be reused repeatedly and indefinitely to remove unwanted objects from valuable slots in the GEO belt. The entire deorbit maneuver will demonstrate toggled control of a satellite's semi-major axis, eccentricity, inclination, and GEO belt longitude. The TugSat concept will ultimately provide a low-cost, long-term, and reusable solution for GEO belt clean up.

Nomenclature

a	=	semi-major axis, km
A	=	surface area, km^2
e	=	eccentricity
i	=	inclination, rad
J	=	cost function
λ	=	longitude, rad
m	=	mass, kg
$\hat{\boldsymbol{n}}$	=	sail surface normal unit vector
ν	=	true anomaly, rad
μ	=	gravitational parameter, $\frac{\mathrm{km}^3}{\mathrm{s}^2}$

r = position magnitude, km
$\boldsymbol{r}$ = position vector, km
ω = angular velocity $\frac{\text{rad}}{\text{s}}$
ϕ = phase angle, rad
$\boldsymbol{\sigma}$ = state error
θ = angle between sail surface normal and sun position vectors, rad
u = argument of latitude, rad
v = velocity magnitude, $\frac{\text{km}}{\text{s}}$
$\boldsymbol{v}$ = velocity vector, $\frac{\text{km}}{\text{s}}$
V = candidate Lyapunov function
$\mathbf{x}$ = state column vector (matrix notation)
$\boldsymbol{\zeta}$ = orbital element parameter vector
$\oplus$ = Earth
$\leftmoon$ = moon
$\odot$ = sun

1. Introduction

Orbital debris accumulation is a topic of growing interest as the number of artificial satellites increases each year. Spent rocket bodies and dead satellites litter Earth orbits, threatening interference with operational satellites or increased fragmentation due to debris-to-debris collision. At geosynchronous equatorial orbits (GEO), debris accumulation is not as severe as that present at low-Earth orbits (LEO); however, GEO is operationally more restrictive due to its narrow dimensions. The Inter-Agency Space Debris Coordination Committee (IADC) has defined the dimensions of the GEO region as presented in Table 1 [1, 2]. Satellites in this region do not experience atmospheric

Table 1: Protected GEO Belt Region

Property	Value
GEO Altitude	35,786 km
Lower Altitude	GEO-200km
Upper Altitude	GEO$+200$km
Inclination	± 15 degrees

drag, so abandonment of assets in the GEO belt poses an indefinite problem for geostationary operations. It is common practice to deorbit end-of-life satellites to graveyard orbits above the GEO belt; however, orbital debris runs the risk of reentering the GEO belt due to the effects of solar radiation pressure (SRP). For these reasons, the IADC also establishes unique deorbit guidelines for satellites in the GEO belt, which are presented in Table 2 [1, 2]. Unfortunately, only about a third of end-of-life GEO satellites have been able to meet these recommendations as the vast majority of satellites experience subsystem failures over their lifetimes [3, 4]. The Galaxy 15 incident is a highly publicized example of the orbital debris problem at GEO and the potential impact of space congestion on satellite operations [5]. As Galaxy 15 drifted through the GEO belt, multiple satellites were at risk of collision, some having to perform avoidance maneuvers. Though control was eventually regained for Galaxy 15, for many satellites, this is not possible.

Table 2: GEO Region Disposal Guidelines

Perigee Altitude	$\leq$	GEO + 235 km + $\left(1000 \cdot C_R \cdot \frac{A}{m}\right)$
	235 km:	sum of the upper altitude of the GEO protected region (200 km) and the maximum descent of a re-orbited spaceraft due to luni-solar and geopotential perturbations (35 km).
	C_R:	solar radiation pressure coefficient, $1 \sim 1.5$
	$\frac{A}{m}$:	aspect area to dry mass $\left(\frac{\mathrm{m}^2}{kg}\right)$
Eccentricity	$\leq$	0.003

To address unresponsive satellites, active debris removal methods have been developed to retrieve and deorbit unwanted bodies from orbit. For example, "Space Sweeper" is designed to eject LEO debris by harnessing the momentum exchange of plastic collisions to effectively sling orbital debris into lower orbit for eventual deorbit using atmospheric drag [6]. "GLiDeR" addresses GEO debris through the attraction of charged particles between a reorbiter spacecraft and the unwanted debris; by willfully maintaining an attractive force between the two bodies, GLiDeR can reorbit GEO debris to an acceptable graveyard orbit [7]. The focus of this paper also addresses maintenance of the GEO belt, harnessing SRP as the primary means of propulsion to perform repeated deorbit of orbital debris. The proposed satellite concept, called "TugSat", will use a large, highly reflective solar sail to maneuver a deorbiter satellite, with captured payload, to a disposal orbit beyond the GEO belt. TugSat can then be reorbited to GEO for rendezvous in a desired GEO slot for capture of another drifting payload.

Using environmental forces to enhance satellite operation has been the topic of many works, leading to interesting methods of satellite control ranging from semi-major axis control using the Earth's magnetic field [8] to satellite formation control by means of atmospheric drag [9]. Control of spacecraft in this manner can reduce propellant dependencies, minimize control efforts, or extend satellite lifespans. This paper is concerned with the viability of orbital control of a satellite using the momentum exchange of sunlight. With the absence of atmospheric drag, the next most significant neoconservative perturbation is SRP. The results presented here will prove orbital debris removal can be performed using solar sails; providing free and near infinite delta-V and allowing for repeated characterization of a satellite's orbit by means of semi-major axis, eccentricity, inclination, and longitude control.

Solar radiation pressure has already been proven a capable means of propulsion, especially in the formation of exotic, non-Keplerian orbits or interplanetary transfer orbits [10, 11]. Additional uses for SRP have been proposed for assistance in satellite disposal for low-Earth orbits [12] or medium Earth orbits (MEO) [13], as well as escape from geosynchronous orbits [14]. These maneuvers are achieved by aligning a solar sail to alter a satellite's orbital velocity to raise or lower the satellite's altitude. Specific strategies for changes in semi-major axis and eccentricity are given in [15], illustrating appropriate satellite orientations throughout the orbit, based on the relative position between the spacecraft and the sun. It is clear from these findings that acceleration and velocity vector geometries play a key role in controlling the effect of applied SRP forces. This research presents a geometrical method for optimizing the rates of change

in the orbital elements and illustrates how the proposed method can be used to perform more advanced maneuvers such as orbital debris removal. To address the challenge of satellite placement into orbital slots in the GEO belt, the control techniques will also be used to perform targeting of GEO belt longitudes. Longitude targeting will allow solar sailing satellites to maneuver between desired regions in the GEO belt.

The current state of the art in solar sailing technology is demonstrated with such examples as JAXA's IKAROS spacecraft [16], The Planetary Society's LightSail-1 [17], and NASA's Sunjammer [18]. JAXA's IKAROS in particular is the first satellite to use solar radiation pressure as its primary means of propulsion and is capable of attitude and orbit control using a high performance solar sail. LightSail-1 was a 3U CubeSat which successfully deployed a highly reflective, 32 m^2 solar sail in LEO before tumbling back into Earth's atmosphere after seven days of orbit. Sunjammer boasts the largest solar sail ever constructed, weighing 32 kg with a 38 m $\times$ 38 m solar sail and surface area over 1200 m^2. With these satellites in mind, other ambitious uses for solar sailing satellites are presented in the body of this study.

The TugSat concept introduces a propellant-less deorbit method using a nonlinear, Lyapunov-inspired controller. This controller produces sail orientations capable of tracking desired semi-major axis, eccentricity, inclination, and longitude values. This is achieved by optimizing time derivatives for the satellite's orbital elements based on the satellite's SRP exposure using the Gaussian variation of parameters (VOP) equations. Key geometric relationships between the satellite's acceleration and orbital velocity vectors will dictate the implementation of these optimized sail orientations. These orientations are validated using Monte Carlo simulations. Ultimately, through a combination of sail-based maneuvers, the TugSat simulation will demonstrate deorbit of defunct satellites from the GEO belt, as well as placement of the deorbiter satellite into desired slots within the GEO belt.

The remainder of the paper is organized as follows: Sec. II introduces the dynamics of a satellite operating at geosynchronous altitudes, Sec. III addresses the control techniques employed to manipulate key orbital elements, Sec. IV outlines the TugSat mission concept, and Sec. V provides a summary of the findings presented in the previous sections.

2. Satellite Dynamics Model

2.1. Force Model

The dynamics model for the GEO orbit includes three gravitational contributions and one non-gravitational perturbation. Gravitational influences come from the Earth's gravity, which includes the $C_{2,0}$ and $C_{2,2}$ gravitational harmonic coefficients, and third body perturbations from the moon and sun. Acceleration from the solar radiation pressure is the only non-gravitational perturbation and acts as the control input for the maneuvers presented in Sections III and IV.

The total acceleration acting on the satellite can then be described as

$$\ddot{\boldsymbol{r}} = \ddot{\boldsymbol{r}}_{\oplus} + \ddot{\boldsymbol{r}}_{\leftmoon} + \ddot{\boldsymbol{r}}_{\odot} + \ddot{\boldsymbol{r}}_{\mathrm{SRP}} \tag{1}$$

As illustrated in Montenbruck and Gill [19, p.55], the Earth's gravitational acceleration at GEO is on the order of $10^{-2}\,\frac{\mathrm{km}}{\mathrm{sec}^2}$, with oblateness contributions on the order of $10^{-6}\,\frac{\mathrm{km}}{\mathrm{sec}^2}$ and $10^{-10}\,\frac{\mathrm{km}}{\mathrm{sec}^2}$ for $C_{2,0}$ and $C_{2,2}$ respectively. The effects of the sun and moon exhibit accelerations on the order of $10^{-8}\,\frac{\mathrm{km}}{\mathrm{sec}^2}$. Geostationary satellites, with typical area to mass

ratios on the order of $0.01\ \frac{\text{m}^2}{\text{kg}}$, experience SRP perturbations on the order of $10^{-10}\ \frac{\text{km}}{\text{sec}^2}$. This magnitude poorly competes with the gravitational accelerations; however, by increasing the area to mass ratio of the satellite, the magnitude of the experienced SRP acceleration can increase to match or even overcome the effects of the sun and moon.

The Earth-based accelerations expressed in an Earth-centered, Earth-fixed (ECEF), principal axis coordinate system are

$$\ddot{\boldsymbol{r}}_{\oplus} = 2\omega_{\oplus}\begin{bmatrix} \dot{y} \\ -\dot{x} \\ 0 \end{bmatrix} + \omega_{\oplus}^2\begin{bmatrix} x \\ y \\ 0 \end{bmatrix} - \nabla\Psi \tag{2}$$

with

$$\Psi = -\frac{\mu}{r}\left[1 + \left(\frac{\bar{\alpha}}{r}\right)^2\left\{3C_{2,2}\frac{x^2 - y^2}{r^2} - \frac{1}{2}C_{2,0}\left(1 - 3\frac{z^2}{r^2}\right)\right\}\right] \tag{3}$$

where $\omega_{\oplus}$ is the angular velocity of the Earth, x, y, and z are the satellite's position coordinates in the principal axis coordinate system, and Ψ is the gravitational potential from the Earth, with gravitational parameter μ, mean radius of the Earth $\bar{\alpha}$, gravitational harmonic coefficients $C_{2,0}$ and $C_{2,2}$, and satellite position magnitude r. The principal axis coordinate system is the standard ECEF coordinate system rotated -14.93 degrees about its $\hat{\boldsymbol{z}}$-axis [20]. The behavior of a satellite under the influence of these Earth dynamics is examined in Lara and Elipe [21]. From Vallado [22, p.575], third body perturbations can be modeled as

$$\ddot{\boldsymbol{r}}_k = -\frac{\mu_k}{r_{\oplus k}^3}\left[\boldsymbol{r} - \left\{3\frac{\boldsymbol{r}\cdot\boldsymbol{r}_{\oplus k}}{r_{\oplus k}^2} - \frac{15}{2}\left(\frac{\boldsymbol{r}\cdot\boldsymbol{r}_{\oplus k}}{r_{\oplus k}^2}\right)^2\right\}\boldsymbol{r}_{\oplus k}\right] \tag{4}$$

where μ_k is the gravitational parameter for third body k and $\boldsymbol{r}_{\oplus k}$ is the position vector of third body k (with magnitude $r_{\oplus k}$) as measured from an Earth-centered, inertial (ECI) coordinate system. The ECI expression for acceleration due to SRP is modeled in Montenbruck [19, p.81] as

$$\ddot{\boldsymbol{r}}_{\text{SRP}} = -\kappa P_{\odot}\frac{AU^2}{r_{\odot}^2}\frac{A}{m}\cos\theta\left[(1-\varepsilon)\hat{\boldsymbol{r}}_{\odot} + 2\varepsilon\cos\theta\hat{\boldsymbol{n}}\right] \quad , \quad \theta \in \left[0, \frac{\pi}{2}\right] \tag{5}$$

with the solar radiation pressure magnitude $P_{\odot}$, satellite distance from the sun $r_{\odot}$, astronomical unit AU, shadow coefficient κ (from the moon and the Earth), reflectivity coefficient ε, area to mass ratio $\frac{A}{m}$, and the angle θ between the sun direction vector $\hat{\boldsymbol{r}}_{\odot}$ (as measured from the satellite) and sail surface normal $\hat{\boldsymbol{n}}$. Since the sail normal direction is measured from the surface facing the sun, θ is restricted to values between 0 and $\frac{\pi}{2}$. For Earth orbits, the solar radiation pressure, $P_{\odot}$, is approximately $4.57\text{e-}6\ \frac{\text{N}}{\text{m}^2}$ and can be scaled based on the instantaneous distance between the satellite and the sun ($\frac{AU^2}{r_{\odot}^2}$). Under a few assumptions, $\frac{AU^2}{r_{\odot}^2} \approx 1$, $\kappa = 1$, $\varepsilon = 1$, a characteristic acceleration can be defined as

$$a_c = 2P_{\odot}\frac{A}{m} \tag{6}$$

and Eq. (5) takes the approximate form

$$\ddot{\boldsymbol{r}}_{\text{SRP}} \approx -a_c\cos^2\theta\hat{\boldsymbol{n}}\ ,\ \theta \in \left[0, \frac{\pi}{2}\right] \tag{7}$$

From Equation (7) it is clear that the magnitude of the experienced SRP acceleration directly depends on the orientation of the sail surface normal. The direction of the SRP acceleration can be determined as a result of assuming perfect reflectivity ($\varepsilon = 1$). Due to the specular reflection of incident photons, the satellite will experience an SRP force acting in the direction opposite that of the sail surface normal, thrusting in the $-\hat{\boldsymbol{n}}$ direction. In this way, the SRP force can be directed in any direction negatively aligned with the sun position vector. Sail alignment at $\theta = 0$ (surface normal in-line with the sun position vector) will produce maximum SRP magnitudes, directed away from the sun. Orientations with $\theta = \frac{\pi}{2}$ (sail perpendicular to the sun) experience minimal accelerations, making it possible to "turn off" SRP, assuming negligible accelerations acting on the satellite bus structure. Intermediate orientations will result in SRP accelerations acting in the direction opposite the sail surface normal with decreasing magnitudes as θ approaches $\frac{\pi}{2}$. Figure 1 illustrates the relationship between the experienced SRP force and the sun direction vector.

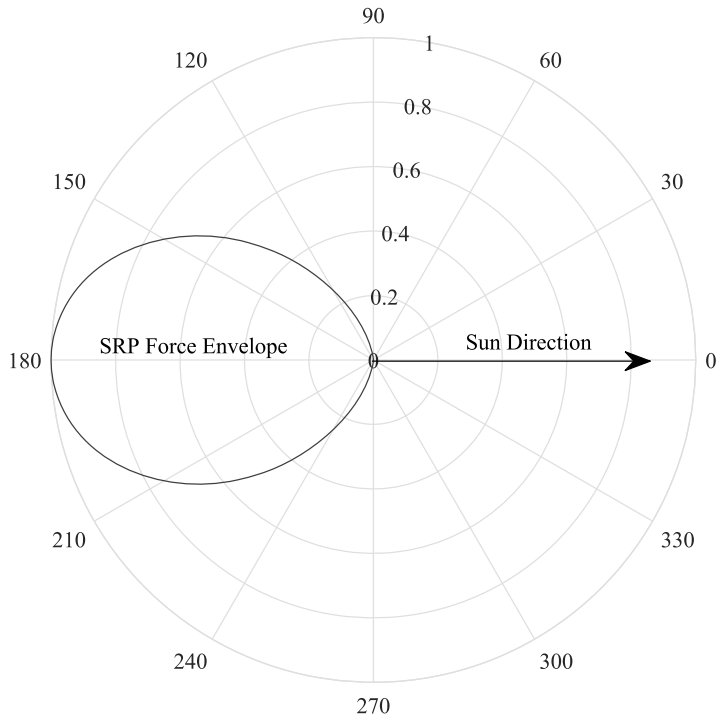

Figure 1: 2-D polar representation of the SRP force envelope based on sun direction. Radial magnitudes are fractions of the maximum available SRP force.

In the upcoming sections, simulations are based off a 50 kg satellite equipped with a perfectly reflective, 800 m^2 (approximately 28 m $\times$ 28 m) solar sail. This area is based on attainable sail sizes and desirable area to mass ratios given the current state of the art for solar sailing satellites. With the additional mass of a 1000 kg payload, the area to mass ratio of the total system is 0.76 $\frac{\mathrm{m}^2}{\mathrm{kg}}$, resulting in a characteristic acceleration of approximately $6.95\text{e-}9$ $\frac{\mathrm{km}}{\mathrm{sec}^2}$ at GEO.

2.2. Gaussian Variation of Parameters

The satellite control logic will make use of time derivatives for the satellite's orbital elements. Expressions for these rates of change can be determined using the Gaus-

sian variation of parameters formulas. These VOP equations are detailed in [22, p.636] and are expressed in the following manner

$$\begin{aligned}
\frac{\mathrm{d}a}{\mathrm{d}t} &= \frac{2}{n\sqrt{1-e^2}}\left\{e\sin(\nu)F_R + \frac{p}{r}F_S\right\} \\
\frac{\mathrm{d}e}{\mathrm{d}t} &= \frac{\sqrt{1-e^2}}{na}\left\{\sin(\nu)F_R + \left(\cos(\nu) + \frac{e+\cos(\nu)}{1+e\cos(\nu)}\right)F_S\right\} \\
\frac{\mathrm{d}i}{\mathrm{d}t} &= \frac{r\cos(u)}{na^2\sqrt{1-e^2}}F_W \\
\frac{\mathrm{d}\Omega}{\mathrm{d}t} &= \frac{r\sin(u)}{na^2\sqrt{1-e^2}\sin(i)}F_W \\
\frac{\mathrm{d}\omega}{\mathrm{d}t} &= \frac{\sqrt{1-e^2}}{nae}\left\{-\cos(\nu)F_R + \sin(\nu)\left(1+\frac{r}{p}\right)F_S\right\} - \frac{r\cot(i)\sin(u)}{h}F_W \\
\frac{\mathrm{d}\nu}{\mathrm{d}t} &= \frac{\sqrt{1-e^2}}{nae}\left\{\cos(\nu)F_R - \frac{2+e\cos(\nu)}{1+e\cos(\nu)}F_S\right\}
\end{aligned} \tag{8}$$

where common notation is used for the orbital descriptors as outlined in the Nomenclature section. The perturbing forces, F_R, F_S, and F_W are components of the specific force vector, $\boldsymbol{F}$, in the LVLH (local vertical, local horizontal) coordinate system with $\hat{\boldsymbol{R}}$ pointing along the position vector of the satellite, $\hat{\boldsymbol{S}}$ in the orbit plane perpendicular to $\hat{\boldsymbol{R}}$ and in the direction of satellite motion, and $\hat{\boldsymbol{W}} = \hat{\boldsymbol{R}} \times \hat{\boldsymbol{S}}$. Equation (8) can be written in matrix form as the product of two matrices $\mathbf{Z}$ and $\mathbf{F}$, defined as

$$\mathbf{Z}(\mathbf{x}) = \begin{bmatrix}
\frac{2}{n\sqrt{1-e^2}}e\sin(\nu) & \frac{2}{n\sqrt{1-e^2}}\frac{p}{r} & 0 \\
\frac{\sqrt{1-e^2}}{na}\sin(\nu) & \frac{\sqrt{1-e^2}}{na}\left(\cos(\nu) + \frac{e+\cos(\nu)}{1+e\cos(\nu)}\right) & 0 \\
0 & 0 & \frac{r\cos(u)}{na^2\sqrt{1-e^2}} \\
0 & 0 & \frac{r\sin(u)}{na^2\sqrt{1-e^2}\sin(i)} \\
-\frac{\sqrt{1-e^2}}{nae}\cos(\nu) & \frac{\sqrt{1-e^2}}{nae}\sin(\nu)\left(1+\frac{r}{p}\right) & -\frac{r\cot(i)\sin(u)}{h} \\
\frac{\sqrt{1-e^2}}{nae}\cos(\nu) & -\frac{\sqrt{1-e^2}}{nae}\frac{2+e\cos(\nu)}{1+e\cos(\nu)} & 0
\end{bmatrix} \tag{9}$$

and

$$\mathbf{F} = \begin{bmatrix} F_R & F_S & F_W \end{bmatrix}^T \tag{10}$$

resulting in

$$\dot{\mathbf{x}} = \mathbf{Z}(\mathbf{x})\,\mathbf{F} \tag{11}$$

where

$$\mathbf{x} = \begin{bmatrix} a & e & i & \Omega & \omega & \nu \end{bmatrix}^T \tag{12}$$

The rows of the $\mathbf{Z}$ matrix can be thought of as row vectors, $\zeta_q(\mathbf{x})$, corresponding to a specific orbital element $q \in \{a, e, i, \Omega, \omega, \nu\}$.

$$\zeta_q(\mathbf{x}) = \begin{bmatrix} \zeta_{q,R} & \zeta_{q,S} & \zeta_{q,W} \end{bmatrix} \tag{13}$$

$$\mathbf{Z} = \begin{bmatrix} \zeta_a^T & \zeta_e^T & \zeta_i^T & \zeta_\Omega^T & \zeta_\omega^T & \zeta_\nu^T \end{bmatrix}^T \tag{14}$$

These expressions describe how the satellite responds to perturbations acting on an otherwise Keplerian orbit. Note the coupling among the various orbital elements.

3. Lyapunov-Inspired Control

As described in the previous section, the exerted SRP force can only oppose the sun position vector($\hat{\boldsymbol{r}}_{\text{SRP}} \cdot \hat{\boldsymbol{r}}_{\odot} < 0$). This adds a significant performance constraint by removing any solutions requiring a control input with a positive SRP force component along the sun position vector. To add further complications, the force magnitude is not uniform across all sail angles, $\theta \in \left[0, \frac{\pi}{2}\right]$. These constraints result in underactuated, low-thrust satellite maneuvering. Given these complex, nonlinear equations and stringent constraints, formulation and solution as a direct optimal control problem is considered infeasible. As a result, the developed method will address control of a satellite's orbital elements individually, accepting any coupled effects on the remaining orbital elements. Controlling the satellite's orbit in this manner requires careful consideration of the order in which to address each orbital element, and does not result in precise tracking of a desired state. For the TugSat mission in particular, it is only necessary to deorbit, reorbit, and target specific GEO belt slots using SRP. These tasks have broad requirements for a, e, i, and longitude values and no restriction for Ω, ω, and ν values.

Define the state error, $\boldsymbol{\sigma}$, as the difference between the actual and desired state.

$$\boldsymbol{\sigma} = \mathbf{x} - \mathbf{x_d} = [\sigma_a \quad \sigma_e \quad \sigma_i \quad \sigma_\Omega \quad \sigma_\omega \quad \sigma_\nu]^T \tag{15}$$

Individual errors for the state variables will be denoted σ_q, where q is a specific orbital element. To attain a desired value for orbital element q, a Lyapunov function, V, can be designed as

$$V = \frac{1}{2}\sigma_q^2 \tag{16}$$

with derivative

$$\dot{V} = \sigma_q \dot{\sigma}_q \tag{17}$$

The control input within $\dot{\sigma}_q$ should be designed to make $\dot{V}$ negative definite. This can be achieved by setting $\dot{\sigma}_q$ equal to a scaled negative of σ_q

$$\dot{\sigma}_q = -k\sigma_q \tag{18}$$

with scaling constant $k > 0$, resulting in

$$\dot{V} = -k\sigma_q^2 \tag{19}$$

a negative definite Lyapunov derivative. In the development that follows, the sail orientation angle θ will be determined such that Eq. (18) is achieved, thereby proving convergence of the error σ_q to zero.

From Eq. (8), the orbital element error time derivative can be expressed in the following form

$$\dot{\sigma}_q = \zeta_{q,R} F_R + \zeta_{q,S} F_S + \zeta_{q,W} F_W = \boldsymbol{\zeta}_q \mathbf{F} \tag{20}$$

The specific force $\mathbf{F}$ contains contributions from the gravitational harmonic coefficients, third bodies, and solar radiation pressure. Grouping the gravitational contributions together in $\mathbf{F}_{\text{grav}}$, the specific force can be re-written as

$$\mathbf{F} = \mathbf{F}_{\text{grav}} + \mathbf{F}_{\text{SRP}} \tag{21}$$

resulting in

$$\begin{aligned}\dot{\sigma}_q &= \boldsymbol{\zeta}_q \left(\mathbf{F}_{\text{grav}} + \mathbf{F}_{\text{SRP}}\right) \\ &= \boldsymbol{\zeta}_q \mathbf{F}_{\text{grav}} + \boldsymbol{\zeta}_q \mathbf{F}_{\text{SRP}} \\ &= D + \boldsymbol{\zeta}_q \mathbf{F}_{\text{SRP}}\end{aligned} \tag{22}$$

where D is the disturbance due to the gravitational accelerations and $\mathbf{F}_{\text{SRP}}$ is the specific force due to SRP. The control input can now be determined using $\mathbf{F}_{\text{SRP}}$. Using Eq. (7) to model the specific force due to SRP, Eq. (22) becomes

$$\dot{\sigma}_q = D - \left(a_c \cos^2\theta\right) \boldsymbol{\zeta}_q \hat{\mathbf{n}} \tag{23}$$

where $\hat{\mathbf{n}}$ is the matrix equivalent to $\hat{\boldsymbol{n}}$.

A new coordinate system will now be introduced, to examine vector relationships in $\dot{\sigma}_q$ through reference of the sun direction unit vector $\hat{\boldsymbol{r}}_\odot$ and a VOP vector $\boldsymbol{\zeta}$ made up of the components of $\boldsymbol{\zeta}_q^T$.

New basis vectors are defined as follows

$$\hat{\boldsymbol{e}}_1 = \hat{\boldsymbol{r}}_\odot \tag{24}$$

$$\hat{\boldsymbol{e}}_2 = \frac{\boldsymbol{\zeta} - (\boldsymbol{\zeta} \cdot \hat{\boldsymbol{r}}_\odot)\,\hat{\boldsymbol{r}}_\odot}{\|\boldsymbol{\zeta} - (\boldsymbol{\zeta} \cdot \hat{\boldsymbol{r}}_\odot)\,\hat{\boldsymbol{r}}_\odot\|} \tag{25}$$

$$\hat{\boldsymbol{e}}_3 = \hat{\boldsymbol{e}}_1 \times \hat{\boldsymbol{e}}_2 \tag{26}$$

In this coordinate system, an angle α is formed between $\hat{\boldsymbol{e}}_1$ and the projection of $\hat{\boldsymbol{n}}$ in the $\hat{\boldsymbol{e}}_1$-$\hat{\boldsymbol{e}}_2$ plane, an angle β is formed between $\hat{\boldsymbol{e}}_1$ and $\boldsymbol{\zeta}$, and an angle δ is formed between the $\hat{\boldsymbol{e}}_1$-$\hat{\boldsymbol{e}}_2$ plane and $\hat{\boldsymbol{n}}$. These relationships are illustrated in Figure 2. The

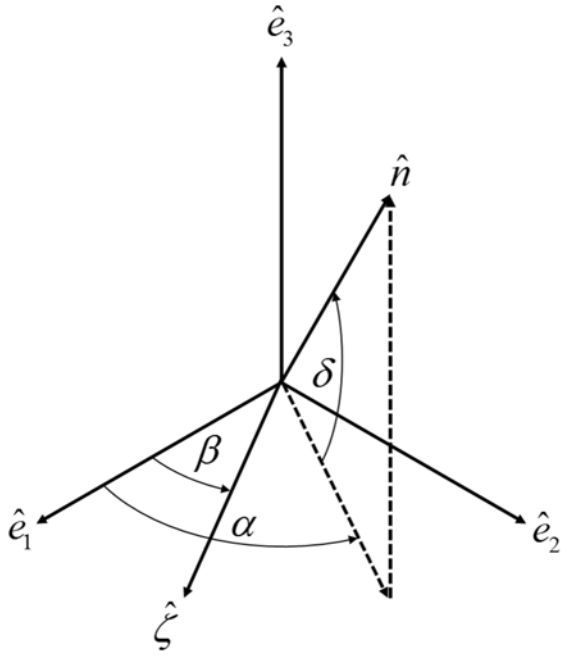

Figure 2: Illustration of vector relationships for optimized sail orientation.

SRP force expressed in terms of angles α, β, and δ is now given as follows

$$\hat{\boldsymbol{n}} = \cos\alpha\cos\delta\hat{\boldsymbol{e}}_1 + \sin\alpha\cos\delta\hat{\boldsymbol{e}}_2 + \sin\delta\hat{\boldsymbol{e}}_3 \tag{27}$$

$$\hat{\boldsymbol{r}}_\odot \cdot \hat{\boldsymbol{n}} = \cos\alpha\cos\delta \tag{28}$$

$$\boldsymbol{\zeta} \cdot \hat{\boldsymbol{n}} = \|\boldsymbol{\zeta}\|\left[\cos\beta\cos\alpha\cos\delta + \sin\beta\sin\alpha\cos\delta\right] \tag{29}$$

where $\|\boldsymbol{\zeta}\|$ is the magnitude of the parameter vector $\boldsymbol{\zeta}$. Rewriting Eq. (23) in terms of Eqs. (27-29) results in

$$\begin{aligned}\dot{\sigma}_q &= D - a_c\|\boldsymbol{\zeta}\|\cos^3\delta\left[\cos^2\alpha\left(\cos\alpha\cos\beta + \sin\alpha\sin\beta\right)\right] \\ &= D - \rho\cos^3\delta\left[\cos^2(\alpha)\cos(\alpha-\beta)\right]\end{aligned} \tag{30}$$

where ρ is the product of the characteristic acceleration a_c and the VOP vector magnitude $\boldsymbol{\zeta}$. To calculate the extrema of Eq. (30), it is required that $\cos\delta = 1 \rightarrow \delta = 0$; restricting $\hat{\boldsymbol{n}}$ to the $\hat{\boldsymbol{e}}_1$-$\hat{\boldsymbol{e}}_2$ plane and resulting in

$$\hat{\boldsymbol{n}} = \cos\alpha\hat{\boldsymbol{e}}_1 + \sin\alpha\hat{\boldsymbol{e}}_2 \tag{31}$$

Since $\hat{\boldsymbol{r}}_\odot \cdot \hat{\boldsymbol{n}} \geq 0$, it follows that $\alpha \in [-\pi/2\ ,\pi/2]$. A cost function *J* can now be defined as

$$J = \cos^2(\alpha)\cos(\alpha-\beta) \tag{32}$$

which can be used to optimize Eq. (30) and yield instantaneous maximum rates of change in $\dot{\sigma}_q$. With β determined by the sun position vector $\hat{\boldsymbol{e}}_1$ and the parameter vector $\boldsymbol{\zeta}$, α is the only controllable angle in *J*. As a result, the solution space for potential control inputs varies periodically as the satellite orbits the Earth. The desired α angle can be determined over the range $[-\pi/2\ ,\pi/2]$, which either minimizes or maximizes *J*. Equation (31) will give the desired sail orientation using the optimized α angle. Using Eq. (32), instantaneous maximum or minimum rates of change can be attained for the satellite's orbital elements.

The task of targeting a desired orbital element value can be achieved by equating Eq. (18) and Eq. (30), resulting in

$$-k\sigma_q = D - \rho\cos^3(\delta)\cos^2(\alpha)\cos(\alpha-\beta) \tag{33}$$

Isolating the α terms, Eq. (33) produces

$$\frac{D + k\sigma_q}{\rho} = \cos^3(\delta)\cos^2(\alpha)\cos(\alpha-\beta) \tag{34}$$

with $\cos^3(\delta)\cos^2(\alpha)\cos(\alpha-\beta)$ bounded between $[-1, 1]$. Recalling that D, ρ, and β are dictated by geometry, values for k, δ, and α must be determined to achieve Eq. (34). Here, a problem arises which halts the formulation of a true Lyapunov controller. Regardless of the design of the scaling constant k, no guarantees can be made to bound the left side of Eq. (34) between $[-1, 1]$ due to the uncertainty (in both sign and relative magnitude) of the disturbance D. Methods to address this disturbance will be investigated in a separate study, outside of the scope of this paper.

In this study, the controller will orient the sail to best achieve Eq. (34). First, $\hat{\boldsymbol{n}}$ will be restricted to the $\hat{\boldsymbol{e}}_1$-$\hat{\boldsymbol{e}}_2$ plane by once again choosing $\delta = 0$. The scaling constant k

is a flexible design choice, chosen to weight control of the error against the effects of D. The updated cost function becomes

$$J = \left| \frac{D + k\sigma_q}{\rho} - \cos^2(\alpha)\cos(\alpha - \beta) \right| \tag{35}$$

to be minimized numerically across the interval $\alpha \in \left[-\frac{\pi}{2}, \frac{\pi}{2}\right]$, as no analytical solution exists for Eq.(35). Though stability of this result cannot be confirmed analytically, the controller will be proven effective through Monte Carlo simulations.

Toggling control between the orbital elements in this manner results in switched system-like behavior. The state evolution can be interpreted to switch between two sets of dynamics: a system under the influence of SRP and a system free of SRP. A nested layer of switching exists within the SRP dynamics, where the sail orientations work to enhance changes in a specific orbital element. In a general sense, the orientations are used to utilize only the desirable effects of the solar radiation pressure. When no desirable SRP contributions exist within a given SRP solution space (e.g., all possible sail orientations result in an increase in semi-major axis when attempting to decrease the satellite's semi-major axis), the solar sail is oriented perpendicular to the incoming sunlight, minimizing the contribution from the SRP force.

4. TugSat

The TugSat simulation will demonstrate the potential to remove orbital debris from the GEO belt using a solar sailing satellite. Recall, TugSat is simulated as a 50 kg satellite equipped with an 800 m^2 solar sail, resulting in an area-to-mass ratio of 16 $\frac{\mathrm{m}^2}{\mathrm{kg}}$. In simulation, the satellite will be deorbiting a 1000 kg payload, decreasing the area-to-mass ratio of the total system to 0.76 $\frac{\mathrm{m}^2}{\mathrm{kg}}$. Initialized in equatorial orbit within the GEO belt, TugSat will begin by raising the semi-major axis of its orbit by 350 km. Once the semi-major axis target is achieved, TugSat will begin reducing the eccentricity of its new orbit while maintaining an altitude above the IADC guidelines for graveyard orbits. Next, TugSat will release the 1000 kg payload and begin descent back to the GEO belt, targeting a desired GEO belt longitude for rendezvous with another payload. These maneuvers will be executed using sail orientations produced by the Lyapunov analysis and implemented under the full dynamics model as described in Section II. The following simulations will expand upon the TugSat maneuvers while demonstrating switched-control of the semi-major axis, eccentricity, inclination, and longitude.

4.1. Semi-Major Axis

The first goal for deorbit using TugSat is to increase the semi-major axis of the payload. An increase in the semi-major axis will result in an increase in the satellite's apogee and a net increase in the satellite's average orbital altitude. For tracking of a desired semi-major axis, a_d, the Lyapunov function is written as

$$\begin{aligned} V &= \frac{1}{2}\sigma_a^2 \\ &= \frac{1}{2}(a - a_d)^2 \end{aligned} \tag{36}$$

with

$$\begin{aligned} \dot{V} &= \sigma_a \dot{\sigma}_a \\ &= (a - a_d)\,\dot{a} \end{aligned} \tag{37}$$

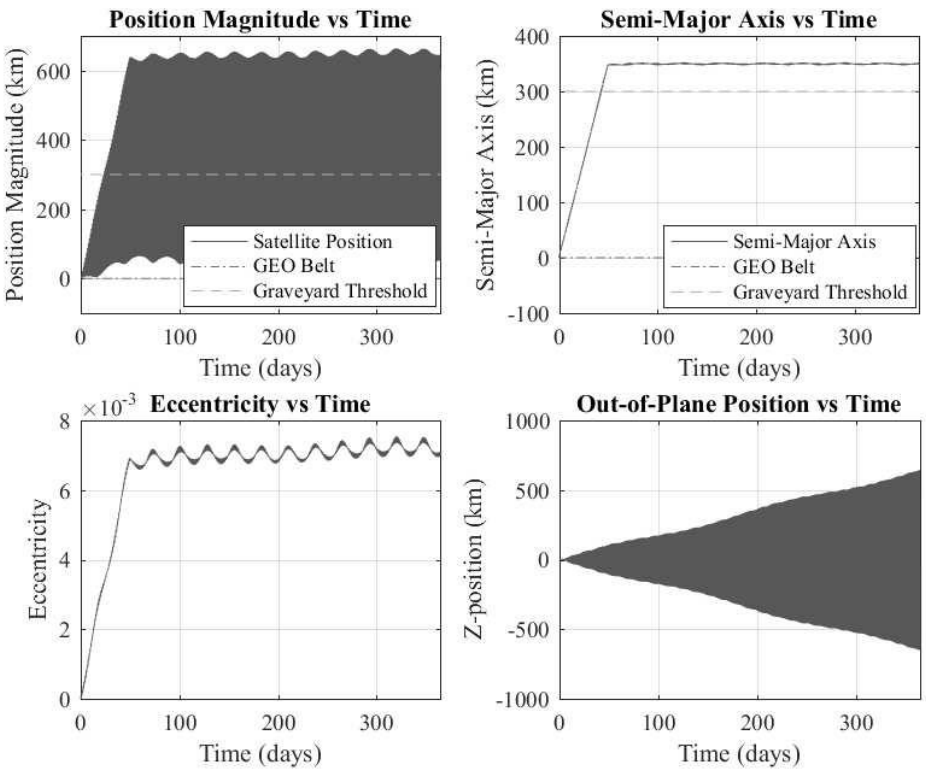

Figure 3: Sail orientations to increase the semi-major axis. Position and semi-major axis values are zeroed at the GEO belt.

The expression for $\dot{a}$ is known from Eq. (8) and the semi-major axis error can be found using the methods described in Section III. Implementing the semi-major axis orientations results in the behaviors illustrated in Figure(3).

To verify the reliability of these orientations, 1000 simulations were performed to target a desired semi-major axis. These simulations were configured using uniformly randomized initial conditions as detailed in Table 3. These initial conditions place the

Table 3: Simulation Properties for Semi-Major Axis Control Tests

Orbital Elements		Range
a_0	semi-major axis	42,164 km
e_0	eccentricity	$\in [0, 0.005]$
i_0	inclination	$\in [-0.0175, 0.0175]$ rad
Ω_0	right ascension of the ascending node	$\in [0, 2\pi]$ rad
ω_0	argument of perigee	$\in [0, 2\pi]$ rad
ν_0	true anomaly	$\in [0, 2\pi]$ rad
a_d		$a_0 \pm 500$ km

Note: Simulation durations of 1 year, initialized between the years 2000 and 2020

satellite within 200 km of the GEO altitude and 1 degree latitude of the GEO slot. All

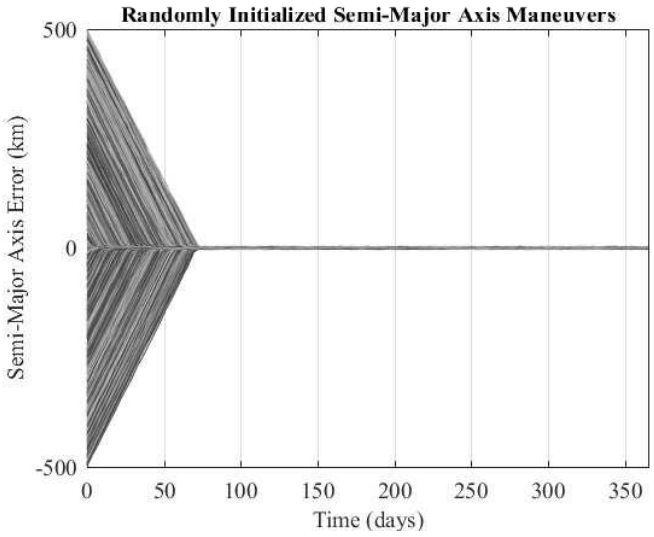

Figure 4: Performance results of 1000 simulations to target desired semi-major axis.

simulations result in successful error convergence as illustrated in Figure (4).

4.2. Eccentricity

Once the desired semi-major axis is attained, the eccentricity must be reduced so that both perigee and apogee values remain above the graveyard orbit threshold. Two methods are now presented.

4.2.1. Greedy Approach

The Lyapunov function corresponding to eccentricity control is

$$\begin{aligned} V &= \frac{1}{2}\sigma_e^2 \\ &= \frac{1}{2}\left(e - e_d\right)^2 \end{aligned} \tag{38}$$

with

$$\begin{aligned} \dot{V} &= \sigma_e \dot{\sigma}_e \\ &= \left(e - e_d\right)\dot{e} \end{aligned} \tag{39}$$

where e_d is the desired eccentricity. The expression for $\dot{e}$ is known from Eq. (8) and the sail orientations to minimize the eccentricity error can be found using the methods described in Section III. Implementing these orientations can reduce the eccentricity as illustrated in Fig. (5).

To validate these orientations, 1000 simulations were executed with initial conditions described in Table 4 below. As displayed in Fig. (6), eccentricity values can be reduced to steady-state values of around $e = 1.75 \times 10^{-3}$, corresponding to a difference of 160 km between apogee and perigee using these orientations.

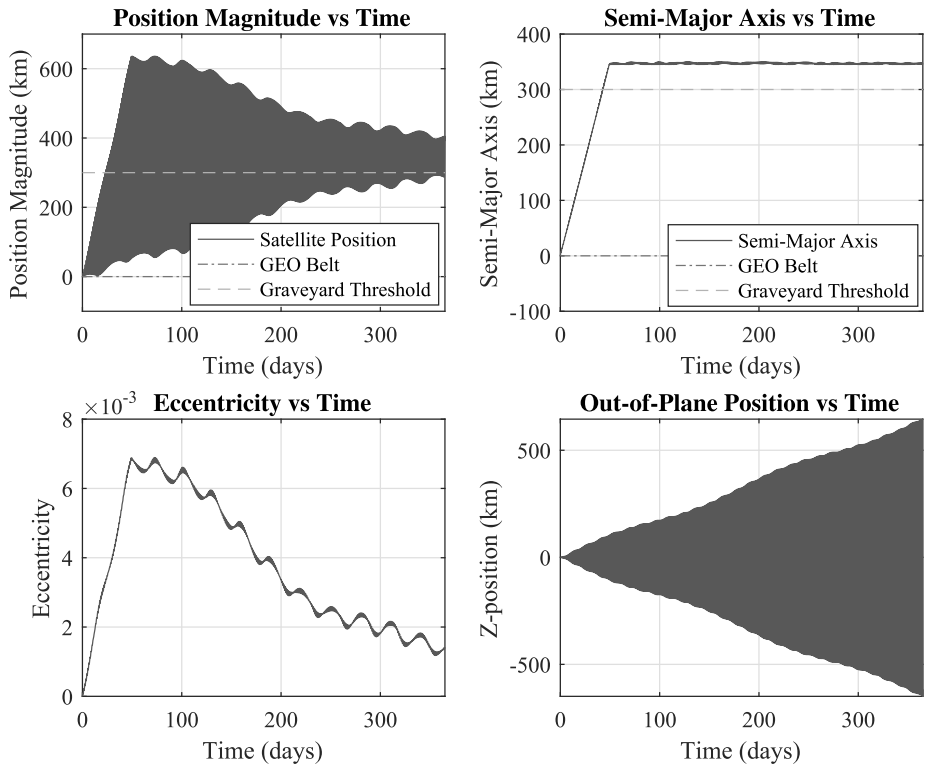

Figure 5: Sail orientations to minimize eccentricity after raising semi-major axis. Position and semi-major axis values are zeroed at the GEO belt.

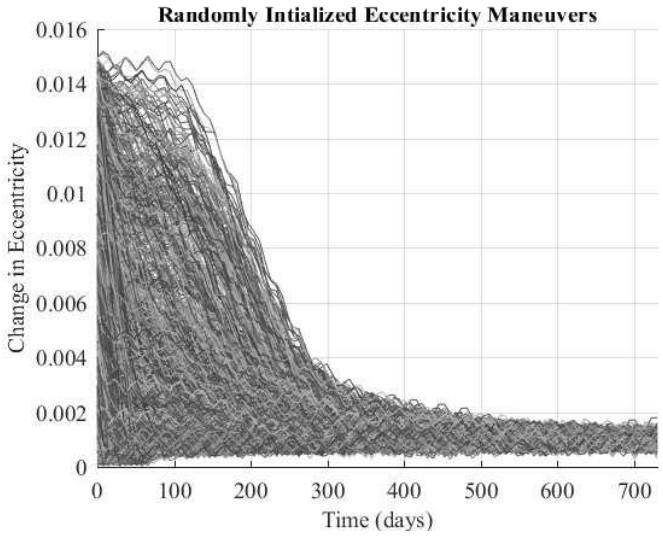

Figure 6: Performance results of 1000 simulations to reduce eccentricity.

Table 4: Simulation Properties for Eccentricity Reduction Tests

Parameter	Range
a_0	$42,164 \pm 500$ km
e_0	$\in [0, 0.015]$
i_0	$\in [-0.0175, 0.0175]$ rad
Ω_0	$\in [0, 2\pi]$ rad
ω_0	$\in [0, 2\pi]$ rad
ν_0	$\in [0, 2\pi]$ rad
e_d	0

Note: Simulation durations of 2 years, initialized between the years 2000 and 2020

4.2.2. Velocity Monitoring

For smaller $\frac{\mathrm{A}}{\mathrm{m}}$, eccentricity reduction using SRP can be improved through a partnering with the existing gravitational accelerations. Recall that the satellite dynamics are dominated by these gravitational effects. These accelerations persist and cannot be controlled; however, their effects on the satellite orbit can be enhanced using SRP. In simulations it was noted that if the eccentricity control was modified as follows, a lower transient response resulted.

To begin, note the characteristic velocity of a circular orbit (neglecting perturbations) in terms of semi-major axis and gravitational parameter:

$$v_\mathrm{circular} = \sqrt{\frac{\mu}{a}} \tag{40}$$

By polling the orbital velocity, it can be determined whether to accelerate or decelerate the satellite by comparing the velocity to the value given by Eq. (40). Solar radiation pressure can be used to amplify the desirable effects from the gravitational accelerations, accelerating or decelerating the satellite as necessary. A velocity-monitoring algorithm is now presented, to determine when to implement the eccentricity orientations for improved reduction of eccentricity:

$$\begin{aligned}
&\textbf{if} \\
&\quad \boldsymbol{v} \cdot \boldsymbol{a}_\mathrm{gravity} > 0 \quad \text{and} \quad \boldsymbol{v} \cdot \hat{\boldsymbol{r}}_\odot < 0 \quad \text{and} \quad v < v_\mathrm{circular} \\
&\textbf{or} \\
&\quad \boldsymbol{v} \cdot \boldsymbol{a}_\mathrm{gravity} < 0 \quad \text{and} \quad \boldsymbol{v} \cdot \hat{\boldsymbol{r}}_\odot > 0 \quad \text{and} \quad v > v_\mathrm{circular} \\
&\textbf{then} \\
&\quad \hat{\boldsymbol{n}} = \cos\alpha \hat{\boldsymbol{e}}_1 + \sin\alpha \hat{\boldsymbol{e}}_2
\end{aligned} \tag{41}$$

where α is determined using the techniques from Section II and the total gravitational acceleration vector is defined as

$$\boldsymbol{a}_\mathrm{gravity} = \ddot{\boldsymbol{r}}_\oplus + \ddot{\boldsymbol{r}}_\leftmoon + \ddot{\boldsymbol{r}}_\odot \tag{42}$$

This algorithm states that the total gravitational acceleration vector must be in positive alignment with the orbital velocity vector to increase the velocity with SRP, or in negative alignment with the orbital velocity vector to decrease the velocity with SRP.

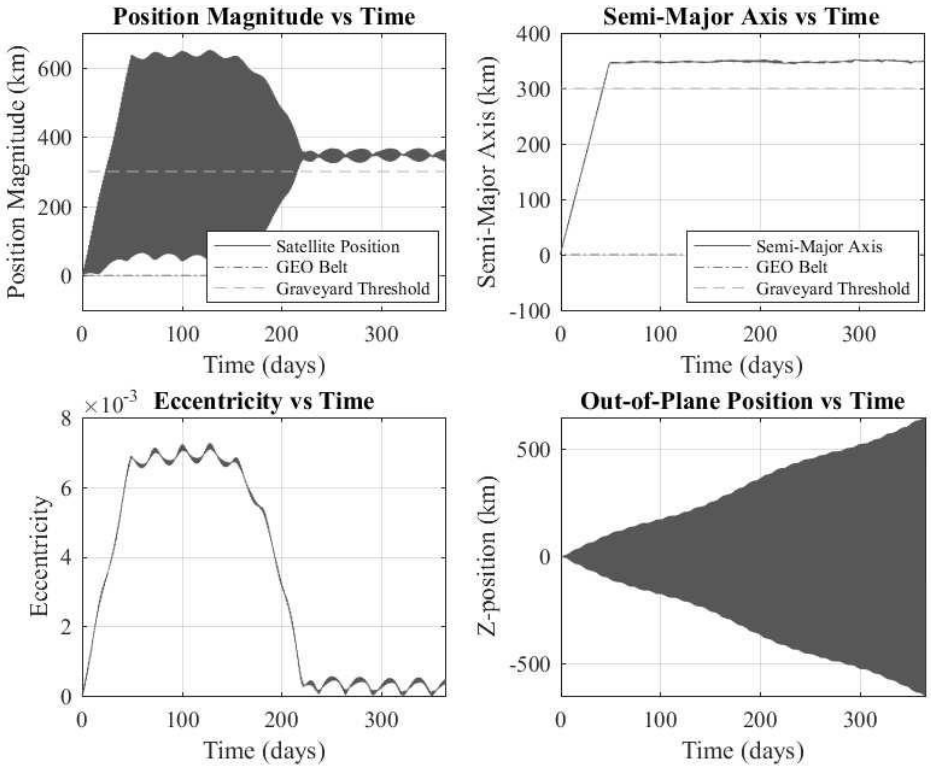

Figure 7: Sail orientations to minimize eccentricity, using velocity monitoring technique, after raising semi-major axis. Position and semi-major axis values are zeroed at the GEO belt.

If neither of the conditions of Eq. (41) are met, the sail normal must be oriented perpendicular to the sun position vector, minimizing the undesirable effects of SRP. The results of this velocity monitoring technique are illustrated in Figure (7). The Monte Carlo analysis for the velocity monitoring technique is displayed in Figure (8) using the same initial conditions from Table 4. Using this method, annual maximum changes in eccentricity of approximately 0.012 are possible. These sharp drops in eccentricity exist in periods of the orbit where beneficial vector alignments exist as outlined in Eq. (41). The plateaus indicate periods of poor alignment between the eccentricity and gravitational acceleration vectors. Steady state error convergence is achieved at eccentricity values of approximately 0.001.

4.3. Inclination

Throughout the orbit, TugSat is exposed to out-of-plane accelerations which create an increase in inclination, leading to oscillations of thousands of kilometers about the equator. While these inclinations are inconsequential during the removal of orbital debris, they can pose problems for rendezvous with a desired orbital slot. To address these drifts, a Lyapunov function can be written as

$$\begin{aligned} V &= \frac{1}{2}\sigma_i^2 \\ &= \frac{1}{2}(i - i_d)^2 \end{aligned} \tag{43}$$

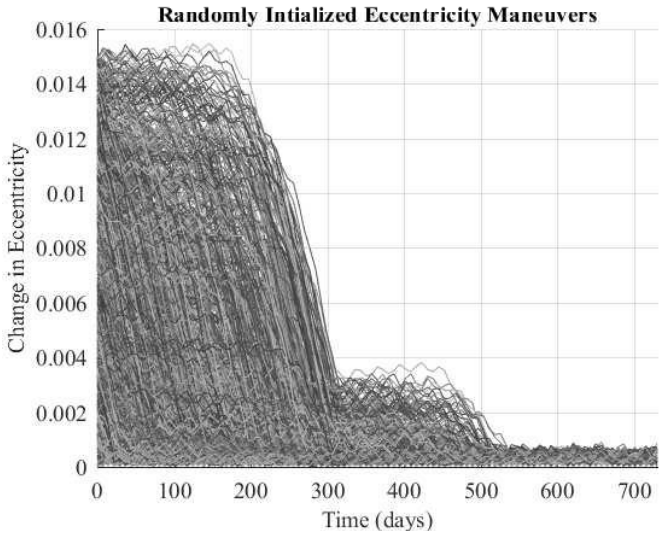

Figure 8: Performance results of 1000 simulations to reduce eccentricity with velocity monitoring.

with

$$\begin{aligned} \dot{V} &= \sigma_i \dot{\sigma}_i \\ &= (i - i_d) \frac{\mathrm{d}i}{\mathrm{d}t} \end{aligned} \tag{44}$$

to determine a control input to achieve the desired inclination, i_d. As before, the expression for $\frac{\mathrm{d}i}{\mathrm{d}t}$ is known from Eq. (8) and sail orientations to minimize the inclination error can be found using the methods described in Section III.

To verify the utility of these orientations, 1000 simulations were executed with initial conditions given in Table 5. For these simulations, the satellite is without payload,

Table 5: Simulation Properties for Inclination Control Tests

Parameter	Range
a_0	42,164 km
e_0	0
i_0	0 rad
Ω_0	$\in [0, 2\pi]$ rad
ω_0	$\in [0, 2\pi]$ rad
ν_0	$\in [0, 2\pi]$ rad
r_z	0 km (inclination of 0 rad)

Note: Simulation durations of 2 years, initialized between the years 2000 and 2020

characterized by an $\frac{\mathrm{A}}{\mathrm{m}}$ ratio of 16 $\frac{\mathrm{m}^2}{\mathrm{kg}}$. The satellite is initialized to drift throughout the GEO belt for 180 days, accumulating inclination changes due to perturbations from Earth's oblateness and third body accelerations. Results of these simulations can be

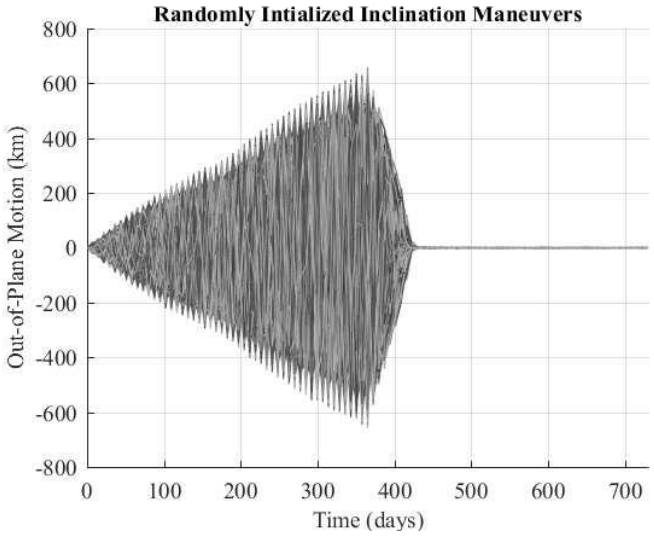

Figure 9: Performance results of 1000 simulations to reduce eccentricity with velocity monitoring.

found in Figure (9), indicating effective reduction of planar-oscillations and return of the satellite to the equatorial plane.

It is important to note that the inclination is only affected by out-of-plane accelerations (those acting along the $\hat{\boldsymbol{W}}$ direction). Solutions producing the desired $\hat{\boldsymbol{W}}$ acceleration may, however, include components in the $\hat{\boldsymbol{R}}$ and $\hat{\boldsymbol{S}}$ directions, potentially affecting the semi-major axis and eccentricity behaviors in an undesirable manner. A geometric work-around is to orient the satellite to only produce accelerations in the $\hat{\boldsymbol{W}}$ direction. This approach may not achieve the desired control input from Eq. (44); however, the resulting orientation will still produce the desired effect as confirmed in simulation. Figure (10) illustrates the return to the equatorial plane using these inclination tracking orientations. Geometries during the spring and fall equinoxes account for the smaller oscillation events on the order of 30 km. Orbits occurring near the equinoxes exhibit oscillations about the equatorial plane due to the geometries of the orbit inclination and the sun direction vector. Favorable geometries simply do not exist for long enough durations during these periods to allow for continuous dampening using only $\hat{\boldsymbol{W}}$ accelerations.

4.4. Longitude Targeting

Once TugSat has released its payload with an acceptable semi-major axis and eccentricity, return to the GEO belt commences. The return orbit requires controlled descent for placement into a desired slot within the GEO belt for rendezvous with another payload. A novel method for longitude targeting using SRP is now presented, utilizing semi-major axis changes and their resulting effects on the satellite's angular velocity.

To begin, the orbital longitude is now defined as

$$\lambda = \omega t \tag{45}$$

where λ is the longitude of interest, ω is angular velocity of the GEO slot, and t is the time since a reference epoch. For circular orbits, the angular velocity is equivalent to

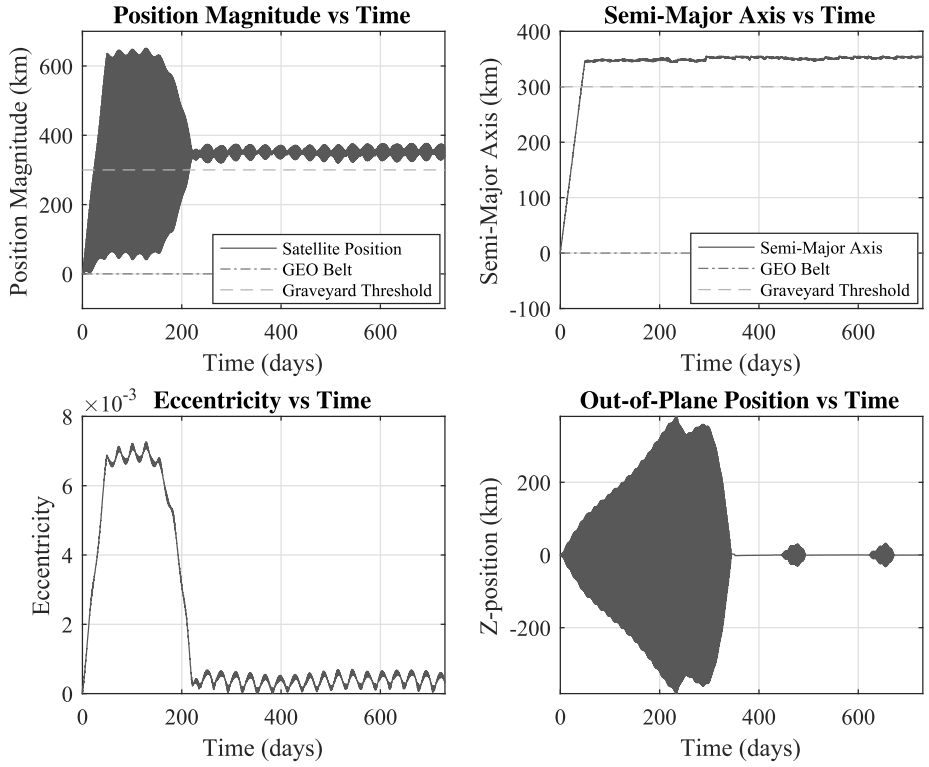

Figure 10: Sail orientations to minimize inclination deorbit and release of payload. Position and semi-major axis values are zeroed at the GEO belt.

the mean motion, n, as follows

$$\omega = n = \sqrt{\frac{\mu}{a^3}} \tag{46}$$

The phase angle, ϕ, between the satellite's longitude and the desired GEO slot longitude will be defined as

$$\phi = \lambda_{\text{satellite}} - \lambda_{\text{slot}} \tag{47}$$

From Eq. (46), it is clear that the angular velocity of a satellite in circular orbit has an inverse relationship with the semi-major axis. With this information, a satellite can speed up to a leading GEO slot by decreasing its semi-major axis or slow down to a trailing GEO slot by increasing its semi-major axis.

To derive Lyapunov-based orientations for longitude targeting, the time derivative of the longitude error ϕ must be expressed as

$$\dot{\phi} = \frac{\mathrm{d}}{\mathrm{d}t}\left(\lambda_{\text{satellite}} - \lambda_{\text{slot}}\right) \tag{48}$$

The angular velocity of the GEO slot is constant, so the time derivative of λ_{slot} is simply the mean motion of the slot, n_{slot}. Due to the small eccentricity of the satellite orbit, the longitude derivative of the satellite will be defined as

$$\dot{\lambda}_{\text{satellite}} = n_{\text{satellite}} \tag{49}$$

resulting in

$$\dot{\phi} = n_{\text{satellite}} - n_{\text{slot}} \tag{50}$$

For longitude control, an $\dot{a}$ term is desired, which can be found by taking one more derivative:

$$\ddot{\phi} = \dot{n}_{satellite} = -\frac{3}{2}\sqrt{\frac{\mu}{a^5}}\dot{a} \tag{51}$$

From these dynamics equations, a controller can be designed to reduce the longitude error using the time derivative of the satellite's mean motion.

The Lyapunov candidate function will be defined as

$$V = \frac{1}{2}\phi^2 + \frac{1}{2}\eta^2 \tag{52}$$

with Lyapunov derivative

$$\dot{V} = \phi\dot{\phi} + \eta\dot{\eta} \tag{53}$$

The η term is a back-stepping error defined as the difference between the satellite's mean motion and the satellite's desired mean motion, n_{d}.

$$\eta = n_{\text{satellite}} - n_{\text{d}} \tag{54}$$

$$\dot{\eta} = \dot{n}_{\text{satellite}} - \dot{n}_{\text{d}} \tag{55}$$

This error will be used in the Lyapunov analysis to drive ϕ to zero using an unmatched control input. To introduce the back-stepping error into the dynamics, Eq. (50) is rewritten as

$$\begin{aligned}\dot{\phi} &= n_{\text{satellite}} - n_{\text{slot}} + n_{\text{d}} - n_{\text{d}} \\ &= \eta - n_{\text{slot}} + n_{\text{d}}\end{aligned} \tag{56}$$

Next, Eq. (51) will be used with Eq. (55), resulting in

$$\dot{\eta} = -\frac{3}{2}\sqrt{\frac{\mu}{a^5}}\dot{a} - \dot{n}_{\mathrm{d}} \tag{57}$$

Inserting these expressions into Eq. (53), the Lyapunov derivative can now be rewritten as

$$\dot{V} = \phi\left(\eta - n_{\mathrm{slot}} + n_{\mathrm{d}}\right) + \eta\left(-\frac{3}{2}\sqrt{\frac{\mu}{a^5}}\dot{a} - \dot{n}_{\mathrm{d}}\right) \tag{58}$$

Equation (58) can be made negative definite through the appropriate design of n_{d} and $\dot{a}$. A suitable design is presented as follows

$$n_{\mathrm{d}} = n_{\mathrm{slot}} - k\phi \tag{59}$$

$$\dot{a} = -\frac{2}{3}\sqrt{\frac{a^5}{\mu}}\left(\dot{n}_{\mathrm{d}} - k\phi - k\eta\right) \tag{60}$$

Combining Eqs. (58-60) results in

$$\begin{aligned}\dot{V} &= \phi\left(k\eta - n_{\mathrm{slot}} + n_{\mathrm{slot}} - k\phi\right) + \eta\left(-\frac{3}{2}\sqrt{\frac{\mu}{a^5}}\left\{-\frac{2}{3}\sqrt{\frac{a^5}{\mu}}\left(\dot{n}_{\mathrm{d}} - k\phi - k\eta\right)\right\} - \dot{n}_{\mathrm{d}}\right)\\ &= -k\phi^2 + k\phi\eta + \eta\left(\dot{n}_{\mathrm{d}} - k\phi - k\eta - \dot{n}_{\mathrm{d}}\right)\\ &= -k\phi^2 + k\phi\eta - k\eta\phi - k\eta^2\end{aligned} \tag{61}$$

ultimately yielding the negative definite Lyapunov derivative:

$$\dot{V} = -k\phi^2 - k\eta^2 \tag{62}$$

Sail orientation angles can be determined by equating Eq. (30) and Eq. (60).

$$\begin{aligned}-\frac{2}{3}\sqrt{\frac{a^5}{\mu}}\left(\dot{n}_{\mathrm{d}} - k\phi - k\eta\right) &= \boldsymbol{\zeta}_a \cdot \boldsymbol{\Gamma}_{\mathrm{SRP}}\\ &= -a_c \left\|\boldsymbol{\zeta}_a\right\| \cos^3\delta\left[\cos^2\alpha\left(\cos\alpha\cos\beta + \sin\alpha\sin\beta\right)\right]\end{aligned} \tag{63}$$

Choosing $\delta = 0$ and recalling the definition of ρ_a as the product of a_c and $\|\boldsymbol{\zeta}_a\|$, Eq. (63) becomes

$$\frac{2\left(\dot{n}_{\mathrm{d}} - k\phi - k\eta\right)}{3\rho_a}\sqrt{\frac{a^5}{\mu}} = \cos^2(\alpha)\cos(\alpha - \beta) \tag{64}$$

Note that for longitude targeting, n_{d} is a constant ($\dot{n}_{\mathrm{d}} = 0$) equal to n_{slot}. The constants on the left-hand side of Eq. (64) can be combined to form ρ_ϕ.

$$\rho_\phi = -\frac{2k\left(\phi + \eta\right)}{3\rho_a}\sqrt{\frac{a^5}{\mu}} \tag{65}$$

A cost function J_ϕ can be expressed as

$$J_\phi = \left|\rho_\phi - \cos^2(\alpha)\cos(\alpha - \beta)\right| \tag{66}$$

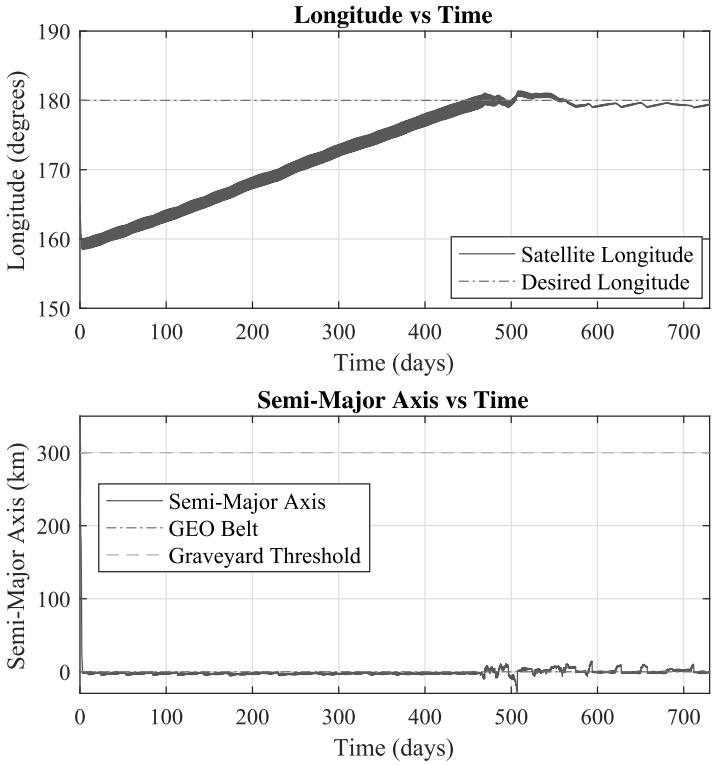

Figure 11: Sail orientations to target desired GEO belt longitude using control of semi-major axis. Semi-major axis values are zeroed at the GEO belt.

As before, the desired orientations can be found by minimizing J_ϕ across the interval $\alpha \in \left[-\frac{\pi}{2}, \frac{\pi}{2}\right]$. With α determined, an algorithm to implement the longitude tracking orientations is presented as

$$\begin{aligned} &\textbf{if} \\ &\quad \phi > 0 \qquad \text{and} \qquad a < a_\text{d} \\ &\textbf{or} \\ &\quad \phi < 0 \qquad \text{and} \qquad a > a_\text{d} \\ &\textbf{then} \\ &\quad \hat{\boldsymbol{n}} = \cos\alpha\hat{\boldsymbol{e}}_1 + \sin\alpha\hat{\boldsymbol{e}}_2 \end{aligned} \tag{67}$$

This algorithm addresses positive phase angles by raising the semi-major axis and negative phase angles by lowering the semi-major axis using orientations produced by the Lyapunov analysis. Figure (11) illustrates longitude targeting using this algorithm.

To gauge the performance of the longitude targeting method, 1000 simulations were run to analyze error convergence and targeting times. Initial semi-major axis values ranged from $\text{GEO} \pm 500$ km and launch dates fell between the years 2000 and 2020. Longitude values were randomized across all angles $\in [0, 2\pi]$. Figure (12) illustrates the results of these simulations. A performance concern is made apparent as a significant percentage of the simulations failed to reach steady state within the 2 year time span. Steady state error convergence was obtained within 2 degrees for

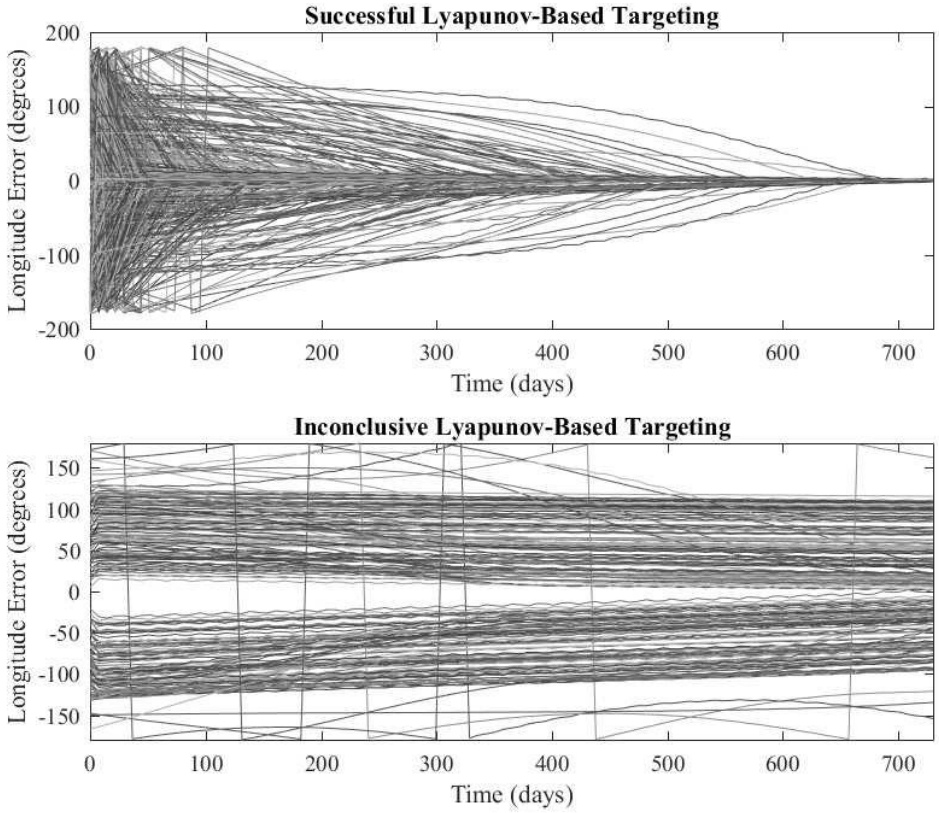

Figure 12: Successful and inconclusive error convergence using longitude targeting method for 1000 simulations. Successful error convergence within 2 years for 80.2% of simulations.

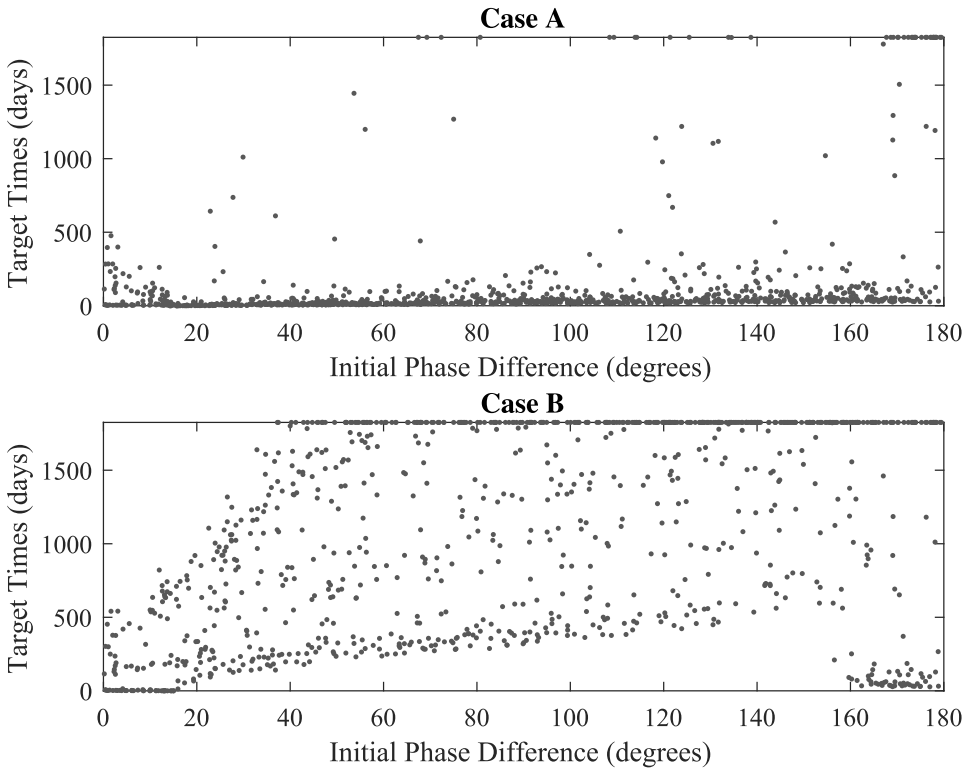

Figure 13: Target times for favorable phase angle and semi-major axis relationships (Case A) and unfavorable phase angle and semi-major axis relationships (Case B).

80.2% of the simulations. To explain the convergence behaviors, targeting scenarios are divided into two cases as described in Table 6. It is observed that targeting ma-

Table 6: Longitude Targeting Cases

Case A	Case B
$\operatorname{sgn}\phi \cdot \operatorname{sgn}(a - a_{\mathrm{d}}) > 0$	$\operatorname{sgn}\phi \cdot \operatorname{sgn}(a - a_{\mathrm{d}}) < 0$

neuvers initialized with longitude and semi-major axis errors corresponding to Case A are capable of error convergence within 2 years. Initial conditions falling under Case B can take over 5 years to achieve error convergence. Figure (13) displays targeting times based on initial phase angles for each case. From these results it is apparent that successful longitude targeting times depend upon the initial relationship between the phase angle and semi-major axis error.

4.5. Deorbit Simulation

With the primary maneuvers outlined, the entire TugSat simulation can be presented. The simulation will begin with TugSat and payload in a perfectly circular, equatorial orbit. Specifically, TugSat will deorbit the payload by increasing the apogee and

raising the semi-major axis 350 km above the GEO altitude. Once the desired semi-major axis is achieved, TugSat will reduce the eccentricity of the orbit before releasing the payload to drift in a disposal orbit as outlined in Table 2. After releasing the payload, Tugsat will return to the GEO belt, targeting its initial longitude from the start of the simulation. This longitude has been chosen arbitrarily in order to demonstrate successful targeting of a desired GEO slot. During rendezvous with the GEO slot, TugSat will reduce its inclination, returning to an equatorial orbit with increased performance due to the increase in the $\frac{A}{m}$ ratio without payload. TugSat will successfully complete its mission upon rendezvous with the targeted GEO slot within the bounds defined in Table 1. Figure (14) displays the TugSat simulation. TugSat successfully deorbits and releases its payload in less than a year. In under a year and a half, TugSat successfully returns to the GEO slot as defined by the IADC. The simulation continues to allow TugSat to further reduce eccentricity and inclination errors. In under two years from the start of the deorbit maneuver, TugSat reduces the out-of-plane motion to within 5 km while maintaining steady-state semi-major axis, eccentricity, and phase error values.

Figures (15) and (16) plot the Lyapunov functions for the TugSat simulation to gauge the performance of the Lyapunov-based sail orientations. These figures analyze the performance during the deorbit and reorbit phases of the simulation. Recall, satellite deorbit does not have inclination or longitude requirements. The Lyapunov functions decrease non-monotonically due to the switching between control of semi-major axis, eccentricity, inclination, and longitude and the presence of the gravitational perturbations. From Figures (15) and (16), the optimized sail orientations prove effective, even under the influence of the full dynamics model.

For this simulation, deorbit and reorbit maneuvers were completed with a delta-V of 0.03 $\frac{\text{km}}{\text{s}}$ and 0.17 $\frac{\text{km}}{\text{s}}$ respectively, without the use of thrusters or propellant. Though the satellite was able to return to the desired GEO location, actual rendezvous with a second payload would require assistance from thrusters for fine maneuvering and successful docking with the payload. By repeating these maneuvers, multiple GEO slots can be made available for reuse using a single solar sailing satellite.

5. Conclusion

Solar radiation pressure serves as a powerful resource for satellites in high altitude orbits, particularly GEO, providing an avenue for low-precision, indefinite satellite maneuvering with virtually infinite delta-V. Control techniques inspired by a Lyapunov analysis, along with the Gaussian variation of parameters equations, produce optimized sail orientations for control of a satellite's orbital elements. Though stability could not be proven analytically, the Monte Carlo results validate the stability of these orientations. Through intelligent switching between control of the orbital elements, the TugSat simulation allows for orbital debris removal and subsequent GEO slot rendezvous in under 2 years without the use of propellants. Supplementing these maneuvers with thrusters for time sensitive, fine maneuvering will greatly enhance the capabilities of a solar sailing mission and open the door for precision rendezvous and docking using solar sailing satellites.

Inspired by the present capabilities of solar sailing technology, the TugSat simulation outlines one potential use for a solar sailing satellite. Small-scale satellites, including CubeSats, are especially suited for such an application. Using a spacecraft on the scale of a 6U CubeSat, sufficient delta-V can be provided to deorbit space

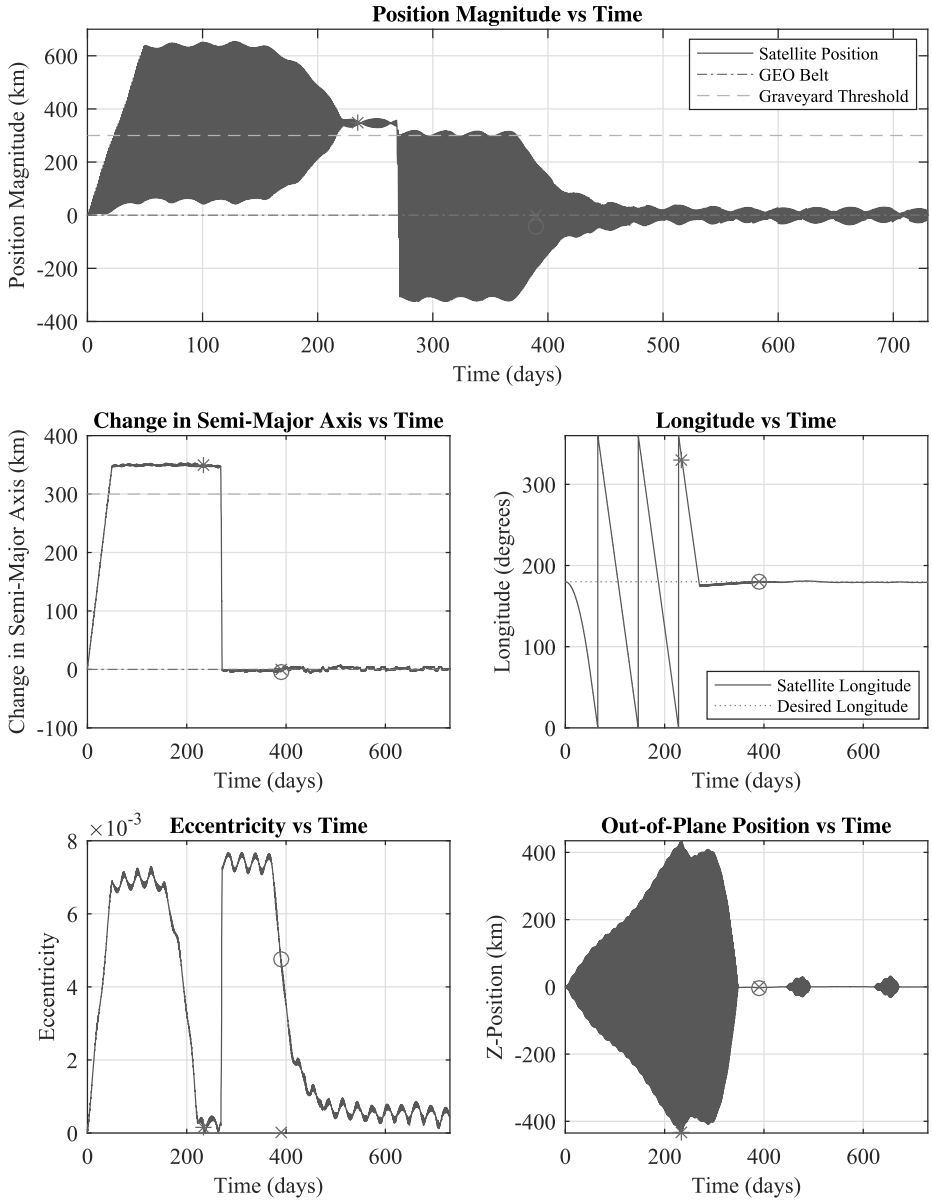

Figure 14: TugSat simulation results. Star denotes release of payload. Circle denotes successful targeting of GEO belt longitude based on IADC guidelines. Cross denotes ideal value for rendezvous.

debris many times more massive than the solar-sailing satellite itself. With the continued trend towards miniaturization, SRP may provide a low-cost, primary means of propulsion for many future satellites.

These findings can be used in future work to investigate optimal, SRP-propelled trajectories for geostationary applications. These techniques may also prove useful for orbit on other celestial bodies where SRP is capable of combating accelerations in a

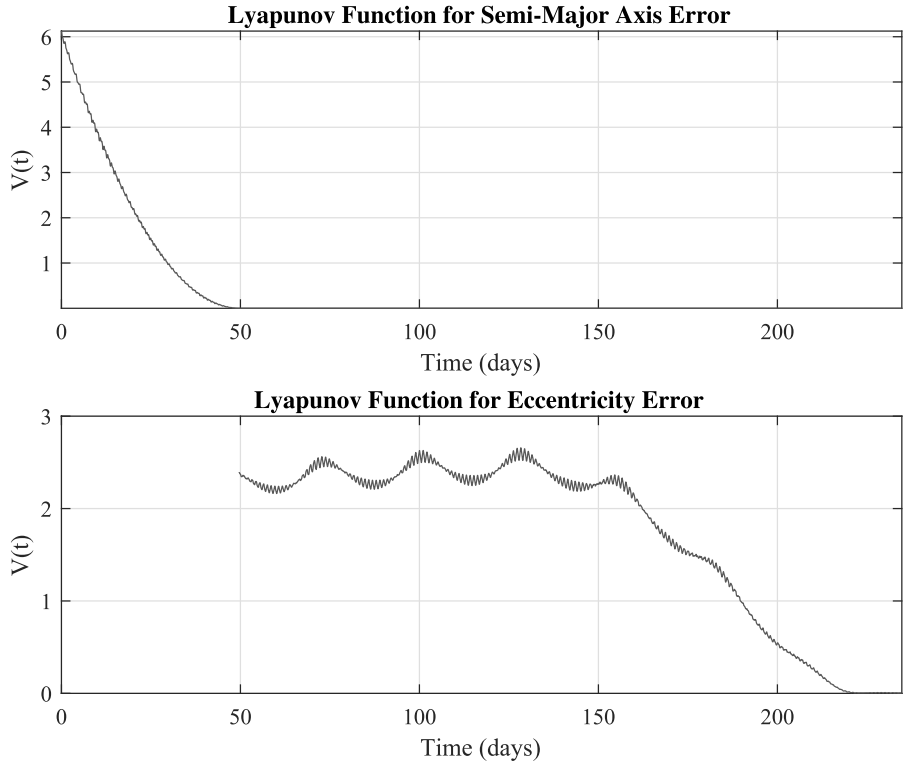

Figure 15: Lyapunov functions during deorbit phase of TugSat simulation.

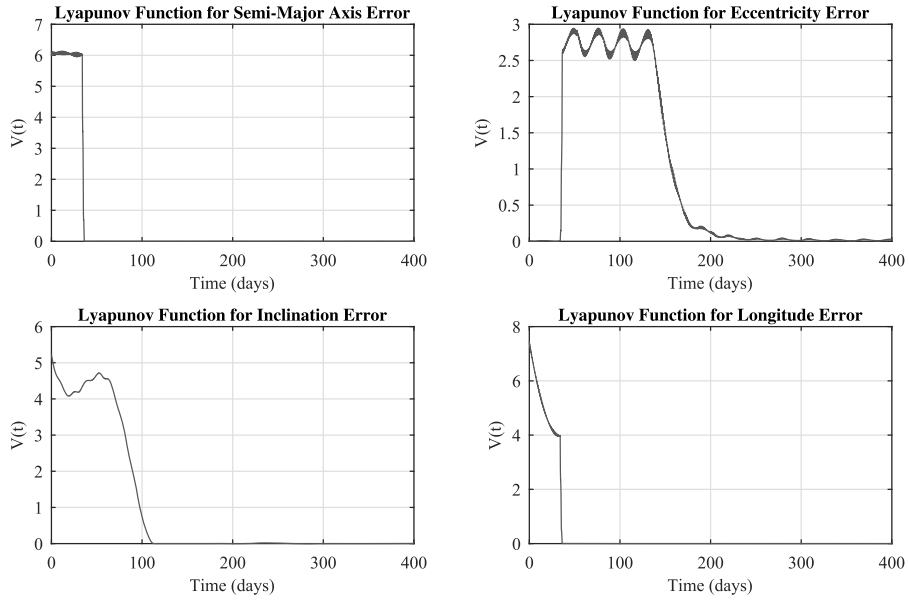

Figure 16: Lyapunov functions during reorbit phase of TugSat simulation.

local environment. Solar sailing can help to reduce propellant dependencies, allowing for the allocation of resources on larger payloads, more sensors, or the elongation of

a satellite's operational lifespan. Using SRP, any number of solar sailing missions can be performed using tactful combinations of these presented maneuvers.

Acknowledgments

The authors would like to thank the Summer Faculty Fellowship Program of the Air Force Research Laboratory and the University of Central Florida (Contract No. 0098313) for sponsoring this investigation.

References

[1] S. Group, W. G. 4, IADC Space Debris Mitigation Guidelines, Technical Report IADC-02-01, Revision 1, Inter-Agency Space Debris Coordination Committee, 2007.
[2] W. G. 4, Support to the IADC Space Debris Mitigation Guidelines, Technical Report IADC-04-06, Revision 5.5, Inter-Agency Space Debris Coordination Committee, 2014.
[3] R. Jehn, V. Agapov, C. Hernández, The situation in the geostationary ring, Advances in Space Research 35 (2005) 1318 – 1327.
[4] J.-F. Castet, J. H. Saleh, Satellite and satellite subsystems reliability: Statistical data analysis and modeling, Reliability Engineering & System Safety 94 (2009) 1718 – 1728.
[5] J. Allen, The galaxy 15 anomaly: Another satellite in the wrong place at a critical time, Space Weather 8 (2010) n/a. S06008.
[6] J. Missel, D. Mortari, Removing space debris through sequential captures and ejections 36 (2013) 743–752.
[7] H. Schaub, D. F. Moorer, Geosynchronous large debris reorbiter: Challenges and prospects, The Journal of the Astronautical Sciences 59 (2012) 161–176.
[8] R. D. Estes, E. C. Lorenzini, J. Sanmartin, J. Pelaez, M. Mart-egrave, C. L. Johnson, I. E. Vas, Bare Tethers for Electrodynamic Spacecraft Propulsion, Journal of Spacecraft and Rockets 37 (2000) 205–211.
[9] R. Bevilacqua, M. Romano, Rendezvous Maneuvers of Multiple Spacecraft Using Differential Drag Under J2 Perturbation, Journal of Guidance, Control, and Dynamics 31 (2008) 1595–1607.
[10] C. R. McInnes, Solar Sailing: Mission Applications and Engineering Challenges, Philosophical Transactions of the Royal Society A: Mathematical, Physical and Engineering Sciences 361 (2003) 2989–3008.
[11] C. R. McInnes, Solar Sailing: Orbital Mechanics and Mission Applications, Advances in Space Research 31 (2003) 1971–1980.
[12] C. Lücking, C. Colombo, C. R. McInnes, Solar Radiation Pressure-Augmented Deorbiting: Passive End-of-Life Disposal from High-Altitude Orbits, Journal of Spacecraft and Rockets 50 (2013) 1256–1267.
[13] C. Lücking, C. Colombo, C. R. McInnes, A Passive Satellite Deorbiting Strategy for Medium Earth Orbit Using Solar Radiation Pressure and the J2 Effect, Acta Astronautica 77 (2012) 197–206.
[14] V. L. Coverstone, J. E. Prussing, Technique for Escape from Geosynchronous Transfer Orbit Using a Solar Sail, Journal of Guidance, Control, and Dynamics 26 (Jul 2003) 628–634.
[15] J. A. Borja, D. Tun, Deorbit Process Using Solar Radiation Force, Journal of Spacecraft and Rockets 43 (2006) 685–687.
[16] Y. Tsuda, O. Mori, R. Funase, H. Sawada, T. Yamamoto, T. Saiki, T. Endo, K. Yonekura, H. Hoshino, J. Kawaguchi, Achievement of IKAROS - Japanese deep space solar sail demonstration mission, Acta Astronautica 82 (2013) 183–188.
[17] C. Biddy, T. Svitek, LightSail-1 solar sail design and qualification, in: Proceedings of the 41st Aerospace Mechanisms Symposium, NASA/CP-2012-217653, pp. 451–463.
[18] J. Heiligers, B. Diedrich, W. Derbes, C. McInnes, Sunjammer: Preliminary end-to-end mission design, in: AIAA/AAS Astrodynamics Specialist Conference, AIAA SPACE Forum, American Institute of Aeronautics and Astronautics, 2014.
[19] O. Montenbruck, E. Gill, Satellite Orbits: Models, Methods and Applications, Springer-Verlag Berlin Heidelberg, New York, 1 edition, pp. 53–116.
[20] H. S. Liu, B. F. Chao, The Earth's equatorial principal axes and moments of inertia, Geophysical Journal International 106 (1991) 699–702.

[21] M. Lara, A. Elipe, Periodic orbits around geostationary positions, Celestial Mechanics and Dynamical Astronomy 82 (2002) 285–299.
[22] D. A. Vallado, Fundamentals of Astrodynamics and Applications, Space Technology Library, Microcosm Press, Hawthorne, CA, fourth edition, pp. 609–730.